Draft version June 19, 2025
Typeset using LaTeX **twocolumn** style in AASTeX631

Asteroseismology of 687 *TESS* Red Giants: Individual Frequencies and Asymptotic Parameters

Jianzhao Zhou(周建召) [1,2] Shaolan Bi(毕少兰) [1,2] Yaguang Li(李亚光) [3] Jie Yu [4,5] Tanda Li(李坦达) [1,2] Xianfei Zhang [1,2] Lifei Ye [1,2] Mengjie Li,[1,2] Liu Long [6] Tiancheng Sun [7] and Yuqin, Chen [1,7]

[1] *Institute for Frontiers in Astronomy and Astrophysics, Beijing Normal University, Beijing 102206, China*
[2] *School of Physics and Astronomy, Beijing Normal University, Beijing 100875, People's Republic of China*
[3] *Institute for Astronomy, University of Hawai'i, 2680 Woodlawn Drive, Honolulu, HI 96822, USA*
[4] *School of Computing, Australian National University, Acton, ACT 2601, Australia*
[5] *Research School of Astronomy & Astrophysics, Australian National University, Cotter Rd., Weston, ACT 2611, Australia*
[6] *Department of Physics, Xiangtan University, Xiangtan 411105, Hunan Province, China*
[7] *CAS Key Laboratory of Optical Astronomy, National Astronomical Observatories, Chinese Academy of Sciences, Beijing 100101, China*

ABSTRACT

The individual modes and asymptotic parameters are important characteristics of stellar oscillation. Using *TESS* 2-minute cadence data from Sectors 1–75, we perform asteroseismic analysis of 687 red giants, and provide their oscillation mode parameters. The mode parameters, including frequencies $\nu_{n,l}$, amplitudes $A_{n,l}$, and linewidths $\Gamma_{n,l}$, are obtained through MCMC fitting. The median uncertainty for frequency is $0.047\,\mu$Hz. Using the radial mode frequencies, we calculated the values of $\Delta\nu$, and derived asymptotic parameters (ϵ_p, ϵ_c, $\delta\nu_{0l}$, q, $\Delta\Pi_1$) based on $l = 0, 1, 2$ modes. For red giants with $\Delta\nu > 15.6\,\mu$Hz, there is a weaker correlation between $\delta\nu_{02}$ and $\Delta\nu$, and a stronger mass dependence, compared to stars with lower $\Delta\nu$. Additionally, the ratio $\delta\nu_{02}/\Delta\nu$ presents a pronounced increase with $\Delta\nu$ decrease, as these stars undergo rapid core contraction and their convective envelopes extend deep into the interior. At this stage, the ratio $\delta\nu_{02}/\Delta\nu$ may serve as a robust indicator for diagnosing the location of the convective boundary. Furthermore, the ϵ_c values can be a potential index to distinguish RC and secondary RC stars from RGB stars in *TESS* field.

Keywords: Asteroseismology (1583); Red giants (655); Low mass stars (2050); Stellar evolution (1599)

1. INTRODUCTION

Asteroseismology is a powerful tool for inferring the internal structure of stars (e.g., Christensen-Dalsgaard 1984; Aerts et al. 2010, 2019). Thanks to space missions such as *CoRoT* (Baglin et al. 2006; Auvergne et al. 2009), *Kepler* (Borucki et al. 2010), and *K2* (Howell et al. 2014), which have provided high-precision light curves, tens of thousands of solar-like oscillators have been discovered and studied in detail (e.g., Huber et al. 2010; Hekker et al. 2011; Stello et al. 2013; Huber et al. 2014; Mathur et al. 2016; Yu et al. 2016, 2018). Recently, the *TESS* mission (Ricker et al. 2015), having observed nearly the entire sky, provided hundreds of thousands of red giant oscillators with ν_{max} using 30-minute full-frame images (FFI) (Schofield et al. 2019; Hon et al. 2021; Stello et al. 2022). Additionally, the sample of solar-like oscillators with ν_{max} and $\Delta\nu$ are obtained, including 4,177 stars of Hatt et al. (2023) using 2-minute and 20-second cadence data, and 8,651 stars identified by Zhou et al. (2024) from 2-minute data in Sectors $1-60$. As *TESS* data release, the extensive short-cadence light curves have significantly expanded the number of sample and enhanced the precision of frequency, and will improve our understanding of the post evolved stars.

The oscillation modes of red giants exhibit a regular pattern in their power spectrum, containing rich stellar information (e.g., Huber et al. 2010; White et al. 2011; Stello et al. 2013; Li et al. 2020). In asymptotic theory, the frequencies $\nu_{n,l}$ of pressure (p) modes can be

Corresponding author: Shaolan Bi, Jianzhao Zhou
bisl@bnu.edu.cn, jianzhaozhou@mail.bnu.edu.cn

approximated (Tassoul 1980; Gough 1986):

$$\nu_{n,l} \approx \Delta\nu \left(n_p + \frac{l}{2} + \epsilon_p \right) - \delta\nu_{0l} \quad (1)$$

where $\Delta\nu$ is the large separation, $\delta\nu_{0l}$ is the small separation, and ϵ_p is a dimensionless offset. The small frequency separation ($\delta\nu_{0l}$) is sensitive to the core structure and, therefore, to the stellar age, particularly during the main sequence phase (White et al. 2011). The ratio of small to large separations ($\delta\nu_{0l}/\Delta\nu$), which is more sensitive to the stellar core and less affected by surface effects, is valuable for inversion techniques to accurately determine the internal structure of stars (Roxburgh & Vorontsov 2003; Bétrisey & Buldgen 2022). Additionally, the parameter ϵ_p is sensitive to the lower and upper turning points of a mode (e.g., Gough 1986). When focusing on the three radial modes near $\nu_{\rm max}$, the offset can be defined as ϵ_c, which distinguishes red clump stars from ascending red giant branch stars based on differences in the local frequency derivative of the underlying phase function (Kallinger et al. 2012; Christensen-Dalsgaard et al. 2014; Ong & Basu 2019).

The dipole ($l = 1$) modes in red giants exhibit a complex mixed-mode pattern that deviates from the asymptotic relation (Equation 1). These mixed modes, resulting from the coupling between the pressure mode and gravity (g) mode cavities, carry information from the core and have observable amplitudes at the surface. For instance, the period spacing of g modes can be used to distinguish between hydrogen-shell-burning and helium-core-burning giants (Bedding et al. 2011). Additionally, mixed modes offer valuable insights into the internal physics of stars, such as measure core rotation (Mosser et al. 2012a; Gehan et al. 2018), constraining angular momentum transport (Goupil et al. 2013; Deheuvels et al. 2014; Li et al. 2024), infer internal magnetic fields (Fuller et al. 2015; Stello et al. 2016; Li et al. 2022, 2023a), convective core overshooting (Deheuvels et al. 2020), and derive accurate stellar parameters (Wang et al. 2023).

For red giants, the evolution of individual mode and asymptotic parameters, such as small frequency spacing $\delta\nu_{0l}$, the offset ϵ_p, amplitude, linewidth, period spacing, and coupling factors, has been extensively studied (e.g. Bedding et al. 2010; Huber et al. 2010; Corsaro et al. 2012; Mosser et al. 2017; Vrard et al. 2018; Kuszlewicz et al. 2023). However, due to the Nyquist frequency limitation of 30-minute cadence *Kepler* observations, the sample of low-luminosity red giants remains sparse. The *TESS* 2-minute cadence data overcomes this limitation, offering continuous coverage from the base of the red giant branch (RGB) to the red clump (RC). In this work, based on the sample of 8,617 solar-like oscillators from Zhou et al. (2024), we use *TESS* 2-minute cadence data from Sectors 1–75 to perform individual mode fitting, and extract radial ($l = 0$), dipole ($l = 1$), and quadrupole ($l = 2$) modes.

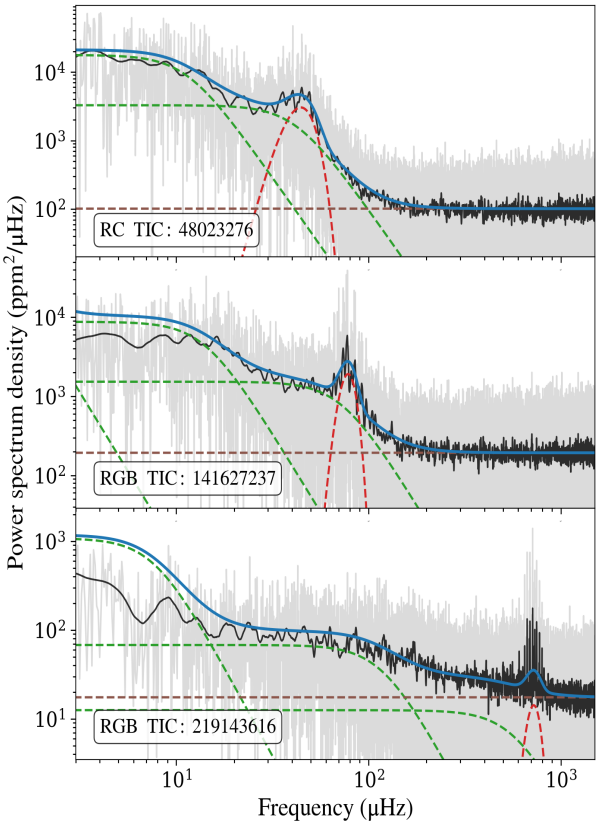

Figure 1. Background fit for the representative stars. The gray line shows the observed power spectrum, while the black line represents the spectrum smoothed using a boxcar filter with a width of 3 μHz. The solid blue line indicates the result of the MCMC fit. The red dashed line shows the fitted Gaussian envelope, the green dashed curve represents the sum of the three Harvey-like components, and the brown straight line corresponds to the white noise level.

2. DATA ANALYSIS

2.1. *Data Preparation*

The sample of red giants was adopted from Zhou et al. (2024), including asteroseismic parameters and background models, which the light curves were extended to Sector 75. All 2-minute cadence light curves were downloaded from the Mikulski Archive for Space Telescopes (MAST) and processed using the *TESS* Science Processing Operations Center (SPOC) pipeline (Jenkins 2017; Twicken et al. 2016). Since the SPOC pipeline has already detrended the data, we only normalized each sector by its mean value before combining all sectors. The

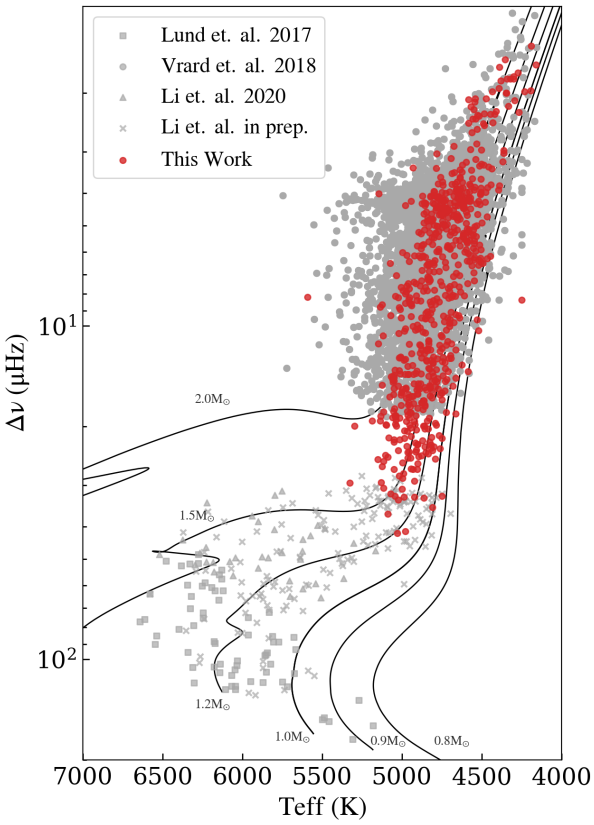

Figure 2. Asteroseismic Hertzsprung-Russell diagram. The gray squares, triangles, and points represent dwarfs, subgiants, and red giants, respectively, from Lund et al. (2017), Li et al. (2020), and Vrard et al. (2018). The gray crosses are from Li et al. (in preparation). The red points represent our sample.

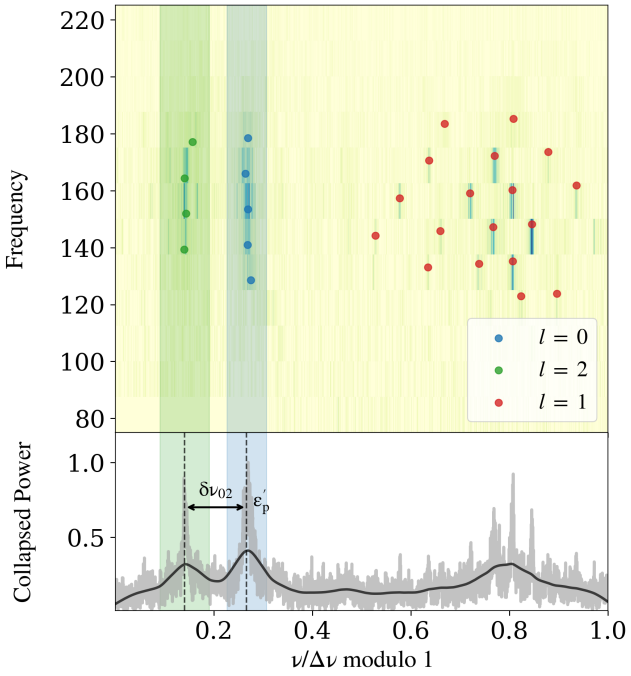

Figure 3. Échelle diagram of TIC 141280255. The blue and green regions correspond to the intervals of $l = 0$ and $l = 2$, respectively. Blue, green, and red points represent $l = 0$, $l = 2$, and $l = 1$ modes. The collapsed power spectrum is normalized by dividing by the maximum value. The two black dashed lines indicate the positions of $\epsilon_p - \delta\nu_{02}$ and ϵ_p, with the distance corresponding to the initial estimate of $\delta\nu_{02}$.

power density spectra of all light curves (PDCSAP data) were transformed using the Lomb-Scargle periodogram method (VanderPlas 2018).

The background model adopted here consists of three Harvey-like profiles to represent granulation components, a constant term for white noise, and a Gaussian envelope to model the oscillation power excess (Chaplin et al. 2014):

$$P(\nu) = \eta(\nu)^2 \left[\sum_{i=1}^{3} \frac{2\sqrt{2}a_i/\pi b_i}{1 + (\nu/b_i)^4} + H_g \exp\left(\frac{-(\nu - \nu_{\max})^2}{2\sigma^2} \right) \right] + W_{\rm n}, \quad (2)$$

where $\eta(\nu) = \mathrm{sinc}\,(\pi\nu/2\nu_{\rm nyq})$ accounts for the frequency-dependent attenuation due to signal discretization, and $\nu_{\rm nyq}$ is the Nyquist frequency (e.g., Chaplin et al. 2011; Kallinger et al. 2014). The parameters a_i and b_i represent the root-mean-square amplitude and characteristic frequency of the i-th Harvey component, respectively. H_g, $\nu_{\max}$, and σ denote the height, central frequency, and width of the Gaussian envelope. $W_{\rm n}$ accounts for the white noise level. The background model fitted to the power spectrum is shown in Figure 1. Subsequently, the spectra were normalized by subtracting the background, in preparation for mode identification and individual mode fitting.

2.2. *Mode Identification*

To identify the oscillation modes for a given star, we first folded the power spectrum by $\Delta\nu$, producing a collapsed power spectrum, and smoothed it by $0.1\Delta\nu$. This spectrum was then cross-correlated with a template to obtain the cross-correlation results, where the template consisted of a Lorentzian profile with a central frequency of 0 and a linewidth of 0.1. Then, we selected the lags corresponding to the three highest cross-correlation factors, within which the central positions of the $l = 0, 2$ modes could be identified. Finally, we computed the differences between these selected lags and determined the initial $\delta\nu_{02}$ values within the range $0.06 < \delta\nu_{02} < 0.3$ based on previous studies (Bedding et al. 2010; Huber et al. 2010; Li et al. 2020). The ϵ_p' was subsequently chosen as the larger value among the selected lags in

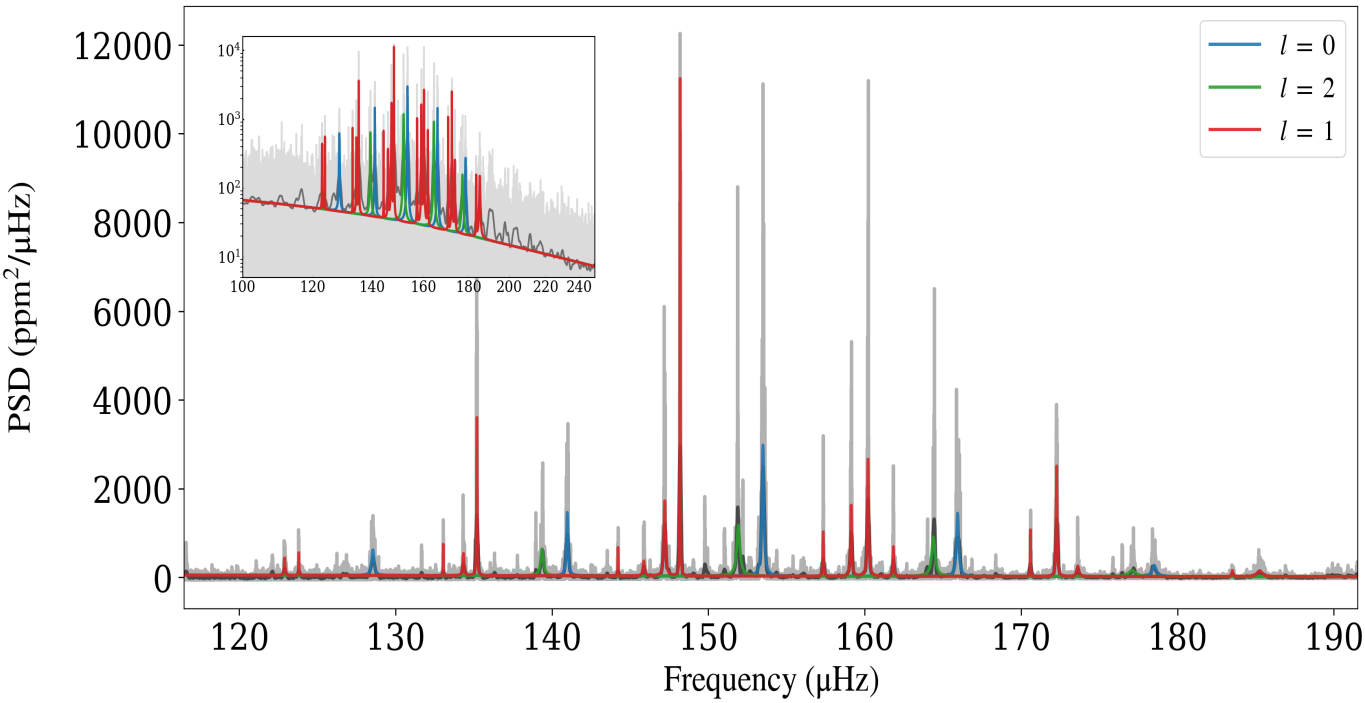

Figure 4. Power spectrum of TIC 141280255. The dark grey line represents the original power spectrum, while the blue, green, and red lines correspond to the fitted results for $l = 0$, $l = 2$, and $l = 1$, respectively.

Table 1. Mode parameters obtained from mode fitting

TIC	l	$\nu_{n,l}$ (μHz)	$A_{n,l}$ (ppm)	$\Gamma_{n,l}$ (μHz)	lnk
1713457	0	145.34 ± 0.22	6.33 ± 0.56	0.85 ± 0.26	10.13 ± 14.43
1713457	0	158.82 ± 0.11	6.67 ± 0.55	0.50 ± 0.14	24.06 ± 14.47
1713457	2	171.29 ± 0.06	–	–	15.05 ± 13.94
1713457	0	172.90 ± 0.09	11.28 ± 0.72	0.49 ± 0.10	120.17 ± 14.08
1713457	2	185.11 ± 0.08	–	–	38.58 ± 14.60
1713457	0	186.81 ± 0.08	11.12 ± 0.78	0.38 ± 0.07	130.92 ± 19.73
1713457	1	194.48 ± 0.18	–	–	16.60 ± 16.28
1713457	2	199.20 ± 0.13	–	–	39.38 ± 16.10
1713457	0	200.86 ± 0.07	9.51 ± 0.74	0.34 ± 0.08	71.96 ± 19.22
1713457	0	214.65 ± 0.22	5.83 ± 0.44	0.99 ± 0.25	13.47 ± 12.84
...	...	...	...	...	...

NOTE—Only the first 10 rows are shown. The full table is available online.

initial $\delta\nu_{02}$, as shown in the bottom panel of Figure 3. The initial ϵ_p is defined as follows (White et al. 2011; Kallinger et al. 2012):

- If $\epsilon'_p < 0.5$ and $\Delta\nu > 3\,\mu$Hz, or if $\Delta\nu > 10\,\mu$Hz, then $\epsilon_p = \epsilon'_p + 1$.
- Otherwise, $\epsilon_p = \epsilon'_p$.

Oscillation modes for l = 0, 1, and 2 were classified based on their positions in the folded power spectrum, following the method in Li et al. (2020). We were selected from peaks with a signal-to-noise ratio (S/N) greater than 3, after smoothing the power spectrum by $0.02\Delta\nu$. Specifically, modes satisfying $(\nu/\Delta\nu \mod 1) \in [\epsilon'_p - 0.04, \epsilon'_p + 0.04]$ were identified as $l = 0$, while those within $[\epsilon'_p - \delta\nu_{02} - 0.05, \epsilon'_p - \delta\nu_{02} + 0.05]$ were labeled as $l = 2$. All remaining modes were provisionally assigned as $l = 1$. These initial mode identifications were visually verified using échelle diagrams, focusing on modes within $\pm 3\Delta\nu$ around $\nu_{\rm max}$, while ensuring that the peaks corresponding to $l = 0, 2$ were identifiable in the folded power spectrum.

Table 2. Stellar Oscillation Parameters

TIC	$\Delta\nu$	ϵ_c	ϵ_p	$d02$	$d01$	q	$\Delta\Pi$	evo$_1$	evo$_2$
21148816	4.43 ± 0.03	0.86 ± 0.16	0.97 ± 0.07	0.58 ± 0.09	–	–	–	1	–
25155698	5.97 ± 0.02	0.94 ± 0.12	1.00 ± 0.04	0.79 ± 0.05	–	–	–	1	–
29762078	1.74 ± 0.02	0.79 ± 0.09	0.78 ± 0.08	0.23 ± 0.03	–	–	–	0	–
29831118	3.86 ± 0.02	0.84 ± 0.10	0.98 ± 0.04	0.54 ± 0.06	–	–	–	1	–
29832379	4.09 ± 0.02	0.96 ± 0.08	0.91 ± 0.03	0.62 ± 0.05	0.21 ± 0.20	0.41 ± 0.10	301.82 ± 0.73	0	1
...	...	...	...	...	...	...	...	...	...
41259424	4.13 ± 0.02	1.00 ± 0.08	0.89 ± 0.03	0.59 ± 0.04	-0.43 ± 0.02	0.29 ± 0.13	250.66 ± 0.70	0	1
48023276	4.54 ± 0.03	0.87 ± 0.17	0.89 ± 0.08	0.73 ± 0.10	-0.08 ± 0.24	0.23 ± 0.14	277.71 ± 4.77	1	1
55366779	2.27 ± 0.01	0.85 ± 0.13	0.71 ± 0.05	0.34 ± 0.03	–	–	–	0	–
55478023	4.54 ± 0.02	0.93 ± 0.07	0.88 ± 0.04	0.60 ± 0.05	0.05 ± 0.05	0.31 ± 0.07	322.02 ± 0.84	1	1
55497082	4.13 ± 0.02	0.97 ± 0.10	0.95 ± 0.04	0.54 ± 0.06	-0.05 ± 0.19	0.32 ± 0.14	277.05 ± 0.53	0	1
...	...	...	...	...	...	...	...	...	...

NOTE—The full table is available online. The parameters evo$_1$ and evo$_2$ represent classifications using ϵ_c and $\Delta\Pi$, respectively. The numerical coding is as follows: 0 – RGB, 1 – RC, 2 – secondary RC, and 3 – AGB.

To ensure sufficient frequency resolution for resolving individual oscillation modes, we required the frequency resolution to be better than 1% of $\Delta\nu$. To further guarantee the reliability of mode identification, we additionally required that the $l = 0$ modes could be clearly distinguished in the échelle diagram. After applying these selection criteria, a total of 687 solar-like oscillators were selected for individual mode fitting, as shown in Figure 2. Among them, only 22 stars have observation durations shorter than 4 sectors, indicating that over 96% of the sample were observed for more than 4 sectors. An example of the mode identification results for TIC 141280255 is shown in Figure 3.

2.3. *Individual Modes Fitting*

The initial identified modes were used as input for individual mode fitting. These modes were modeled using a sum of Lorentzian profiles $L_{nl}(\nu)$:

$$L_{nl}(\nu) = \frac{2A_{nl}^2}{\pi\Gamma_{nl}} \frac{1}{1 + 4\left(\nu - \nu_{nl}\right)^2 / \Gamma_{nl}^2}, \quad (3)$$

where ν_{nl}, Γ_{nl}, and A_{nl} represent the mode frequency, linewidth, and amplitude, respectively (Anderson et al. 1990). In this work, we did not consider the rotational splitting of $l = 1, 2$ modes. Each identified mode was treated as an individual mode for the fitting process. Since $l = 1, 2$ modes are affected by rotational splitting, their amplitudes and linewidths may be unreliable and are therefore not provided here (Corsaro et al. 2015).

To fit the modes, we employed a Markov chain Monte Carlo (MCMC) optimization algorithm using an open-source software package `SOLARLIKEPEAKBAGGING` (Handberg & Campante 2011; Li et al. 2020). The algorithm used uniform priors for the mode frequencies and a modified Jeffreys prior for linewidths and amplitudes. The likelihood function for the fitting process was defined as:

$$\ln p(D|\theta, M) = -\sum_i \left[\ln M_i(\theta) + \frac{D_i}{M_i(\theta)}\right], \quad (4)$$

where D_i is the observed data, $M_i(\theta)$ is the model, and θ is the set of parameters: ν_{nl}, A_{nl}, and Γ_{nl}. The MCMC algorithm yielded the best-fitting values for the frequencies, linewidths, and amplitudes, along with their associated uncertainties. This algorithm also computes the Bayesian factor to assess existence of a mode, defined as $\ln K = \ln p(D|M_1, I) - \ln p(D|M_0, I)$, where H_1 is the hypothesis that a range of the frequency contains the mode, and H_0 is the null hypothesis. To ensure the significance of the modes, we retained only those with $lnk \geq 3$. The power spectrum fitting result for TIC 141280255 is shown in Figure 4. The fitting results are listed in Table 1.

3. ASYMPTOTIC PARAMETERS

3.1. *Estimating $\Delta\nu$, ϵ_p, $\delta\nu_{02}$ and ϵ_c*

For high-radial order p modes, the second-order asymptotic relation can be expressed as,

$$\nu_{p,l} = \left(n_p + \frac{l}{2} + \epsilon_p + \frac{\alpha}{2}(n_p - n_{\max})^2\right)\Delta\nu - \delta\nu_{0l}, \quad (5)$$

where $n_{\max} = \nu_{\max}/\Delta\nu$ is the radial order at the max-power frequency (Mosser et al. 2012b). The parameters $\Delta\nu$, ϵ_p, α, and $\delta\nu_{0l}$ describe the second-order asymptotic behavior of the oscillation frequencies.

To obtain the best-fitting values for the parameters $\Delta\nu$, ϵ_p, α, and $\delta\nu_{02}$, we ran another MCMC optimiza-

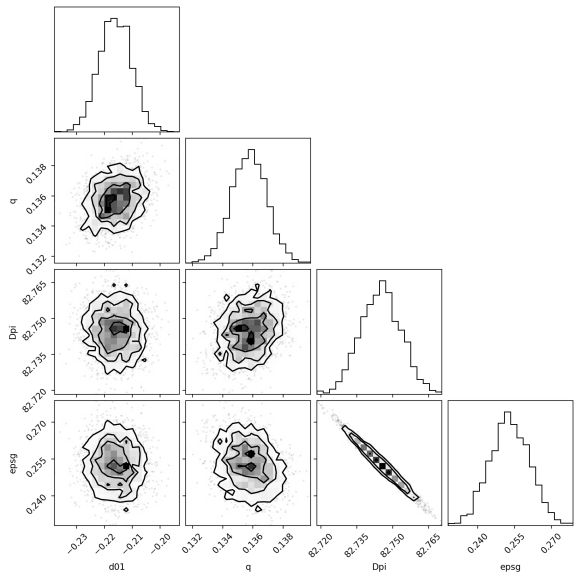

Figure 5. Corner diagram of the posterior distributions of TIC 141280255 by fitting mixed modes.

tion algorithm that fitted the $l = 0, 2$ mode frequencies using Equation 5, implemented in the `emcee` package (Foreman-Mackey et al. 2013). The fitting process maximized the likelihood function L_p, which is defined as:

$$\ln L_p = -\frac{1}{2} \sum_{l=0,2} \sum_i \left[\frac{(\nu_{l,i} - \nu_{p,l,i})^2}{\sigma_{l,i}^2} + \ln(2\pi\sigma_{l,i}^2) \right], \quad (6)$$

where $\nu_{l,i}$ is the observed frequency, $\nu_{p,l,i}$ represents the theoretical frequency, and $\sigma_{l,i}$ is the uncertainty associated with $\nu_{l,i}$. In the MCMC code, we used 32 parallel chains with 2000 steps, retaining the last 1500 steps for the final posterior distributions. The uncertainty for each parameter was determined using the 16% and 84% percentiles of the posterior distribution, corresponding to the 1σ confidence level.

When $\alpha = 0$ in Equation 5, the expression reduces to the first-order asymptotic relation in Equation 1. To ensure the consistence of our results with previous studies, we also fitted the $l = 0, 2$ mode frequencies using the first-order asymptotic relation. Additionally, by fitting the frequencies of the three radial modes closest to $\nu_{\max}$ using the method from Kallinger et al. (2012), we obtained ϵ_c from $\nu_{c,0} = \Delta\nu_c\,(n + \epsilon_c)$. The values of $\Delta\nu$, ϵ_p, $\delta\nu_{02}$, and ϵ_c were listed in Table 2.

3.2. *Estimating* $\delta\nu_{01}$, q, $\Delta\Pi_1$

For pure g-modes, the periods are evenly spaced, and the frequencies $\nu_{\rm g}$ can be expressed as:

$$\frac{1}{\nu_{\rm g}} \approx \Delta\Pi_1\,(n_{\rm g} + \epsilon_{\rm g}) \quad (7)$$

where $\Delta\Pi_1$ is the g-mode period spacing, and $\epsilon_{\rm g}$ is a phase offset.

Mixed mode frequencies can be calculated using the asymptotic relation following as (Shibahashi 1979; Unno et al. 1979):

$$\tan\theta_p = q\tan\theta_g, \quad (8)$$

where q is the coupling factor, which provides insight into the interaction between the radiative core and the hydrogen-burning shell in subgiants and red giants (Mosser et al. 2017). The phase terms θ_g and θ_p, representing pure g-mode and p-mode contributions, are defined as:

$$\theta_g = \pi \frac{1}{\Delta\Pi_1} \left(\frac{1}{\nu} - \frac{1}{\nu_g} \right), \quad (9)$$

$$\theta_p = \pi \frac{\nu - \nu_{p,l=1}}{\Delta\nu}, \quad (10)$$

where ν_g is the g-mode frequency defined by Equation 7, and $\nu_{p,l=1}$ corresponds to the $l = 1$ pure p-mode frequency determined from Equation 5.

To obtain $\delta\nu_{01}$, q, $\Delta\Pi_1$, ϵ_g, we ran a MCMC optimization algorithm to search for the best-fitting parameters of $l = 1$ mixed modes by maximizing the likelihood function:

$$\ln L_{l=1} = -\frac{1}{2} \sum_i \left[\frac{(\nu_i - \nu_{cal,i})^2}{\sigma_i^2} + \ln\left(2\pi\sigma_i^2\right) \right], \quad (11)$$

where ν_i and $\nu_{cal,i}$ are the observed mixed mode frequencies and calculated frequencies from Equation 8, and σ_i is the uncertainty associated with the i-th frequency. We used 32 parallel chains with 2000 steps, retaining the last 1500 steps for the final posterior distributions, as shown in Figure 5. The fitting results for $\delta\nu_{01}$, q, and $\Delta\Pi_1$ are listed in Table 2.

4. RESULT

We performed individual mode fitting for 687 red giants using *TESS* 2-minute cadence data from Sectors 1–75 and extracted $\nu_{n,l}$ for the $l = 0, 1, 2$ modes, as well as $A_{n,l}$ and $\Gamma_{n,l}$ for the $l = 0$ modes. The median uncertainties are 0.047 μHz for $\nu_{n,l}$, 8.5% for $A_{n,l}$, and 26.1% for $\Gamma_{n,l}$, as shown in Figure 6. The fitting results are listed in Table 1.

The fitting was performed using MCMC methods implemented in the open-source software package `SOLARLIKEPEAKBAGGING`, with significance tests and visual inspections ensuring robust mode identification. Using the mode frequencies, we derived the asymptotic parameters $\Delta\nu$, ϵ_p, ϵ_c, $\delta\nu_{0l}$, q, and $\Delta\Pi_1$, as listed in Table 2.

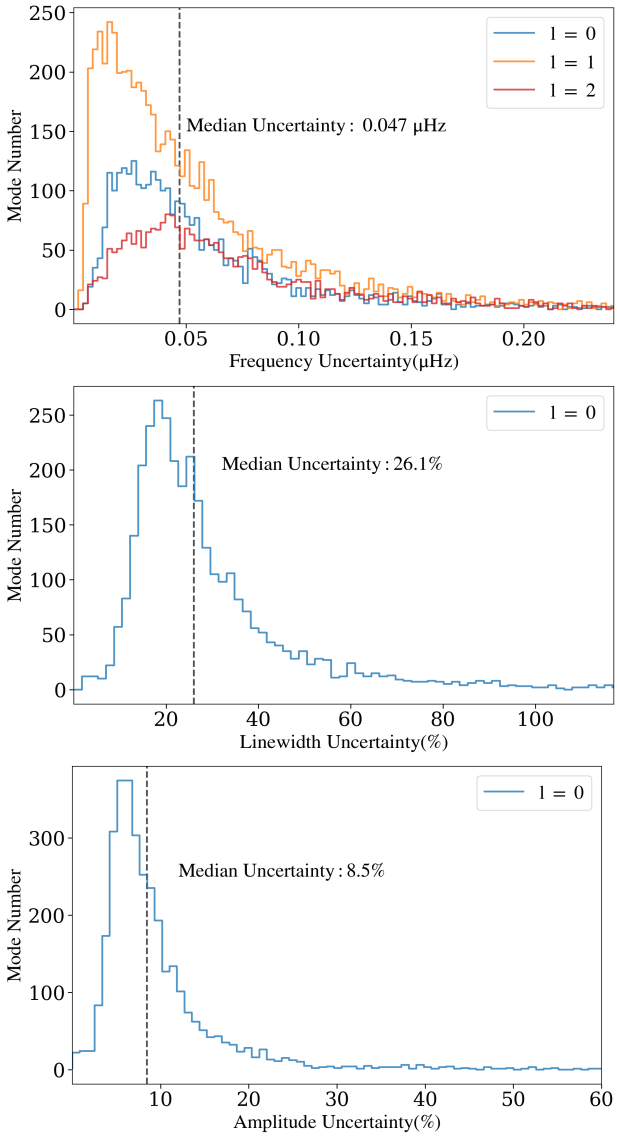

Figure 6. Histograms of the uncertainties for the measured mode frequencies (top), linewidths (middle), and amplitudes (bottom) are shown, with linewidths and amplitudes presented as relative uncertainties.

4.1. $\delta\nu_{02}$ *and the ratio* $\delta\nu_{02}/\Delta\nu$

Figure 7 shows the small frequency separation $\delta\nu_{02}$ versus $\Delta\nu$, known as the $C-D$ diagram (Christensen-Dalsgaard 1984). We find that the distribution of $\delta\nu_{02}$ and $\Delta\nu$ does not follow a single linear relation during the red giant branch, but rather exhibits two distinct segments. For stars with $\Delta\nu < 15.6\,\mu$Hz, there is a strong correlation between $\delta\nu_{02}$ and $\Delta\nu$, with only weak mass dependence, consistent with results from *Kepler* (e.g., Bedding et al. 2010; Huber et al. 2010). However, for $\Delta\nu > 15.6\,\mu$Hz, this correlation weakens, revealing a more pronounced mass dependence.

By performing a piecewise fit to the relation of the form $\delta\nu_{02} = K\Delta\nu + B$ for stars with $\Delta\nu < 15.6\,\mu$Hz and $\Delta\nu \geq 15.6\,\mu$Hz, we obtain the following relations:

$$\delta\nu_{02} = \begin{cases} (0.123 \pm 0.002)\Delta\nu + (0.063 \pm 0.009), \\ \text{for } \Delta\nu < 15.6\,\mu\text{Hz}, \\ (0.073 \pm 0.003)\Delta\nu + (0.090 \pm 0.069), \\ \text{for } \Delta\nu > 15.6\,\mu\text{Hz}. \end{cases} \quad (12)$$

For $\Delta\nu < 15.6\ \mu$Hz, the result is consistent with that of Bedding et al. (2010). For $\Delta\nu > 15.6\ \mu$Hz, the slope 0.073 is smaller than that of $\Delta\nu < 15.6\ \mu$Hz and is close to the fitting result 0.088 for the subgiants of Li et al. (2020). This may suggest differences in the stellar structure of red giants.

To quantify the difference in mass dependence between the two segments, we fit a linear relation for the slope, $K = \alpha + \beta(M/M_{\odot})$, using stellar masses derived from scaling relations. For $\Delta\nu < 15\,\mu$Hz, $\alpha = 0.141 \pm 0.004$ and $\beta = -0.016 \pm 0.003$, which are consistent with those reported by Corsaro et al. (2012). For $\Delta\nu > 15\,\mu$Hz, $\alpha = 0.118 \pm 0.004$, $\beta = -0.050 \pm 0.004$, and the value of the mass-related coefficient β is approximately three times that of the value for stars with smaller $\Delta\nu$.

Figure 8 shows the distribution of the ratio $\delta\nu_{02}/\Delta\nu$ versus $\Delta\nu$. For red giants with $\Delta\nu > 15.6\ \mu$Hz, the ratio $\delta\nu_{02}/\Delta\nu$ exhibits a significant increase with $\Delta\nu$ decrease, due to the rapid deepening of the outer convective envelope until it approaches the compact helium core with a hydrogen-burning shell. For stars with $\Delta\nu < 15.6\ \mu$Hz, the ratio $\delta\nu_{02}/\Delta\nu$ shows a slight increase as $\Delta\nu$ decreases, because the convective envelope have extended sufficiently deep, consistent with the result of Huber et al. (2010). The result suggests that $\delta\nu_{02}/\Delta\nu$ may serve as a robust indicator for diagnosing the location of the convective boundary in red giants with higher $\Delta\nu$, as it reflects the acoustic distance from the stellar center (Ong et al. 2025). Additionally, we compared our sample with *Kepler* data across different evolutionary stages, and found that the RC sequence exhibits slightly higher $\delta\nu_{02}/\Delta\nu$ values than RGB stars, similar to previous findings (Kallinger et al. 2010).

4.2. ϵ_p *and* ϵ_c

Figure 9 (a) presents the $\epsilon_{\rm p}$ versus $\Delta\nu$ diagram. Since $\epsilon_{\rm p}$ is strongly affected by surface effects, there is a systematically offset between the evolutionary models (dashed line) and our sample. To correct for surface effects, we applied a surface correction function in the inverse-cubic form (Osaki & Shibahashi 1990), where the free parameters depend on stellar atmospheric parameters, following the method of Li et al. (2023b). This

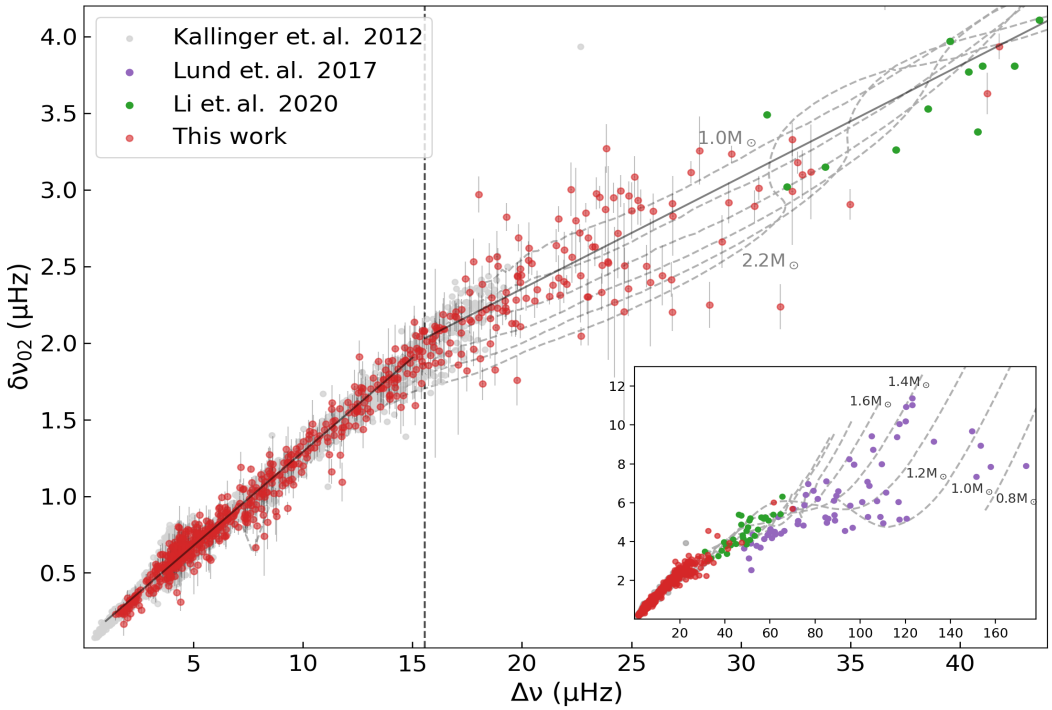

Figure 7. C-D diagram: the ratio $\delta\nu_{02}$ versus $\Delta\nu$. The purple points are MS stars (Lund et al. 2017), the green points are subgiants (Li et al. 2020), the gray points are giants (Kallinger et al. 2012), and the red points are are our sample from *TESS*. The gray dashed lines are the evolutionary tracks for stars with solar metallicity in the mass range of 0.8–2.2 $M_{\odot}$, computed using MESA and GYRE.

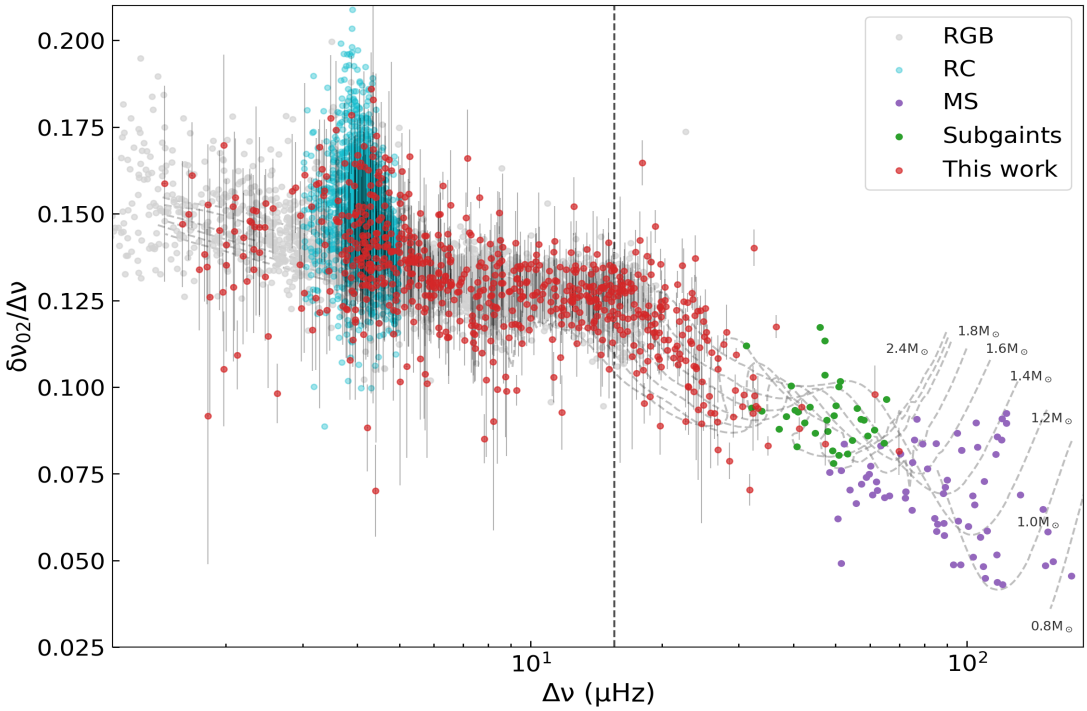

Figure 8. Modified C-D diagram: the ratio $\delta\nu_{02}/\Delta\nu$ versus $\Delta\nu$. The purple points are main-sequence stars (Lund et al. 2017), the green points are subgiants (Li et al. 2020), the light blue and gray points are red clump and red giant branch stars (Kallinger et al. 2012), respectively, and the red points are our sample from *TESS*.

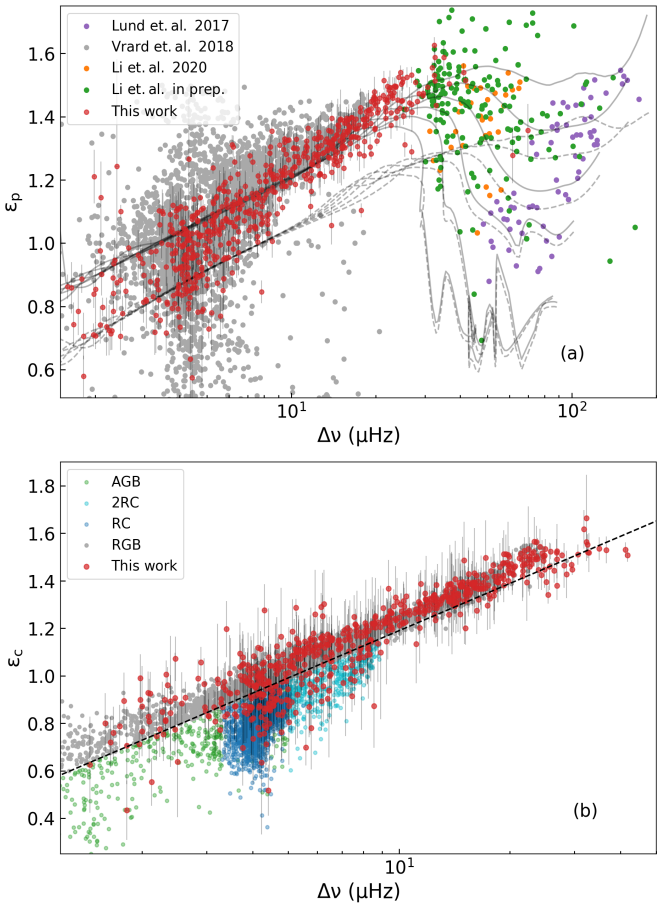

Figure 9. (a) ϵ_p versus $\Delta\nu$ diagram, the gray dashed line shows the model calculations, and the solid line shows the results with surface effect corrections. (b) ϵ_c versus $\Delta\nu$ diagram. The red points are our sample, while the other points are the result from Vrard et al. (2024). The black dashed line corresponds to the relation from Kallinger et al. (2012).

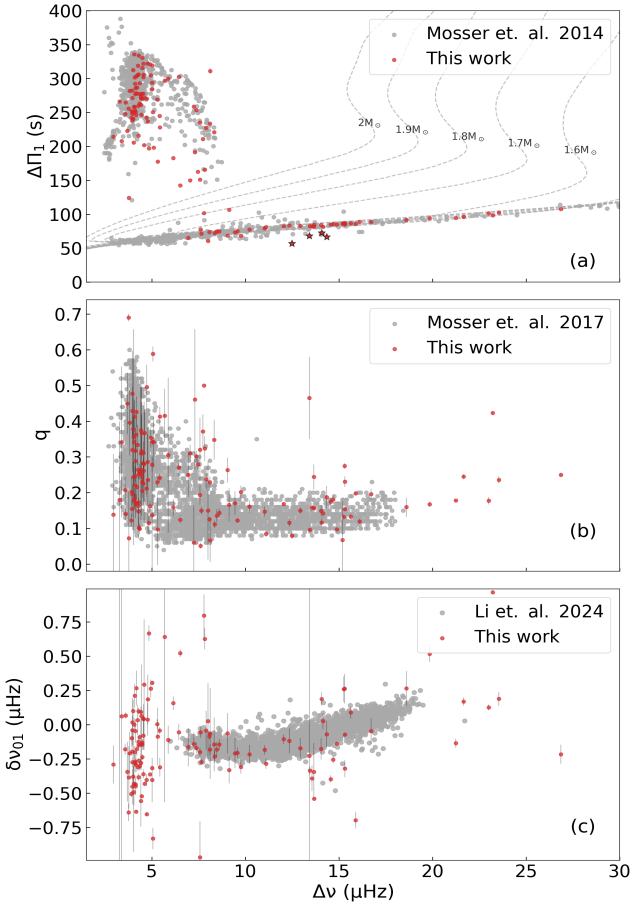

Figure 10. Parameters $\Delta\Pi$, q, and $\delta\nu_{01}$ versus $\Delta\nu$. (a) The dipolar g-mode period spacing $\Delta\Pi$ versus the large separation $\Delta\nu$. (b) The coupling factor q versus $\Delta\nu$. (c) The small frequency separation $\delta\nu_{01}$ versus $\Delta\nu$.

result in the revised models (solid line) aligns well with the observational data. As shown in Figure 9 (a), the ϵ_p exhibits a consistent correlation with $\Delta\nu$ in red giants. We observe that ϵ_p values become more dispersed around $\Delta\nu \sim 5\,\mu$Hz, which may be associated with RC stars.

Figure 9 (b) displays the distribution of ϵ_c and $\Delta\nu$ diagram, combined with the *Kepler* stars (Kallinger et al. 2012). We can see that RC, secondary RC, and asymptotic giant branch (AGB) stars are well distinguished from RGB stars in *Kepler* data. The red giants show a positive correlation between ϵ_c and $\Delta\nu$, while RC, secondary RC and AGB stars lie beneath this trend and exhibit a concentrated distribution at different values of $\Delta\nu$. Our sample exhibits a distribution similar to that of the *Kepler* sample. Using this method, we can classify our sample into RGB, RC, and secondary RC stars, listed in Table 2. The diagram of $\epsilon_c - \Delta\nu$ can be used to distinguish the evolved stars and their evolutionary state. This is because the ϵ_c value represents the difference between RC and RGB in the thermodynamic state of the convective envelope (Christensen-Dalsgaard et al. 2014).

4.3. $\Delta\Pi_1$, q and $\delta\nu_{01}$

Figure 10 (a), (b) and (c) show $\Delta\Pi_1$, q and $\delta\nu_{01}$ versus $\Delta\nu$ diagrams, respectively. A distinct RC sequence concentrates around $\Delta\nu \sim 5\,\mu$Hz. In Figure 10 (a), the red giants display a positive correlation between $\Delta\Pi_1$ and $\Delta\nu$ with $\Delta\Pi_1 \lesssim 120$ s, known as the "degenerate sequence", which corresponds to low-mass ($M < 1.5 M_\odot$) giants with a degenerate helium core (Deheuvels et al. 2022). There are four stars below the degenerate sequence (highlighted points in Figure 10 (a)), which may be due to mass accretion from a stellar companion after they have developed degenerate cores Rui & Fuller

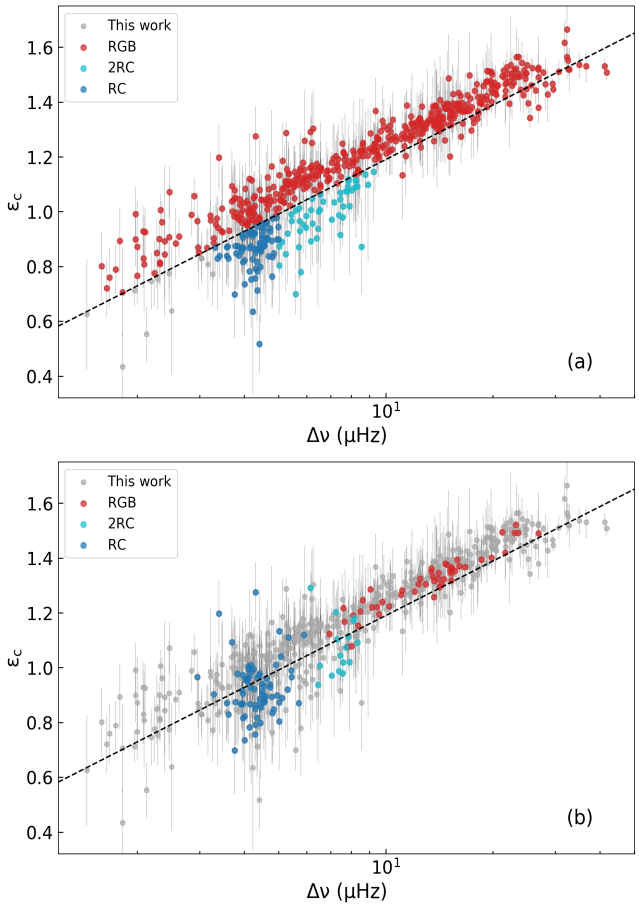

Figure 11. The ϵ_c versus $\Delta\nu$ diagram. (a) The evolutionary stages based on the empirical boundary from Kallinger et al. (2012). (b) The evolutionary stages based on $\Delta\Pi_1$ from this work.

(2021); Deheuvels et al. (2022). In Figure 10 (b) and (c), RGB stars show that both q and $\delta\nu_{01}$ decrease with decreasing $\Delta\nu$, which is consistent with previous studies, although the distribution appears to be somewhat scattered.

4.4. *Classification for Stellar Evolutionary Stages*

We present the classification results of stellar evolutionary stages based on ϵ_c and $\Delta\Pi_1$ in the ϵ_c–$\Delta\nu$ diagram, as shown in Figure 11. The black dashed line represents an empirical boundary that separates red giants from other stars (Kallinger et al. 2012). RGB stars follow a strong correlation with $\Delta\nu$ and are located above this boundary, while RC and secondary RC stars are primarily found below it, as shown in Figure 11(a). In Figure 11(b), approximately half of the RC stars and about one-third of the secondary RC stars classified by $\Delta\Pi_1$ appear above the black dashed line. Only two red giants classified by $\Delta\Pi_1$ fall below the line. These misclassifications occur mainly near the boundary, possibly due to systematic measurement uncertainties or the limited observation durations. All RC stars confirmed by $\Delta\Pi_1$ are also identified using the ϵ_c–$\Delta\nu$ diagram, demonstrating that the ϵ_c–$\Delta\nu$ diagram can partially distinguish RC stars from RGB stars, although some contamination remains within the RGB population.

Since ϵ_c is easier to obtain compared to $\Delta\Pi_1$, using the ϵ_c–$\Delta\nu$ diagram for classifying stellar evolutionary stages is a fast and promising approach. With continued TESS observations, the frequency resolution will improve significantly, leading to more precise estimates of ϵ_c and further enhancing the classification accuracy.

5. CONCLUSIONS

We performed an asteroseismic analysis of 687 red giants using TESS 2-minute cadence data from Sectors 1–75. The individual oscillation modes, including radial, dipole, and quadrupole modes ($l = 0, 1, 2$), are fitted using MCMC methods, with significance tests and visual inspections ensuring robust mode identification. The main conclusions are as follows:

1. We provide frequencies $\nu_{n,l}$ for the $l = 0, 1, 2$ modes, as well as amplitudes $A_{n,l}$ and linewidths $\Gamma_{n,l}$ for the $l = 0$ modes, with a median frequency uncertainty of 0.047 μHz. Based on these frequencies, we derived key asteroseismic parameters, including $\Delta\nu$, ϵ_p, ϵ_c, $\delta\nu_{0l}$, q, and $\Delta\Pi_1$, which serve as strong observational constraints on stellar models.

2. For red giants with $\Delta\nu > 15.6\,\mu$Hz, the relation between $\delta\nu_{02}$ and $\Delta\nu$ shows a stronger dependence on stellar mass and consequently a weaker correlation, compared to stars with lower $\Delta\nu$. Meanwhile, the ratio $\delta\nu_{02}/\Delta\nu$ exhibits a significant increase as $\Delta\nu$ decreases, accompanied by the rapid deepening of the outer convective envelope until it approaches the compact helium core with a hydrogen-burning shell, and shows a different trend for red giants with lower $\Delta\nu$. The result suggests that the ratio $\delta\nu_{02}/\Delta\nu$ may serve as a robust indicator for diagnosing the location of the convective boundary.

3. The RC and secondary RC stars can be distinguished from RGB stars using $\epsilon_c - \Delta\nu$ diagram, although some contamination may still exist. The $\epsilon_c - \Delta\nu$ diagram has the potential to quickly distinguish evolved stars and their evolutionary states. As the duration of TESS observations increases, the classification accuracy will also improve.

This work presents asymptotic parameters covering the $\Delta\nu$ range from 15 to 30 μHz, which will aid in better calibrating them as functions of stellar properties. It provides valuable observational constraints on the internal structures and evolutionary characteristics of red giants. The rotational splitting of mixed modes, an aspect not yet explored in this study, offers a promising opportunity to investigate angular momentum transport and may serve as a potential probe for measuring internal stellar magnetic fields, which we plan to explore in future work.

This work is supported by the National Key R&D Program of China No. 2024YFA1611901, NSFC grants (12090040, 12090042), the Joint Research Fund in Astronomy (U2031203) under cooperative agreement between the National Natural Science Foundation of China (NSFC) and the Chinese Academy of Sciences (CAS), and the CSST project.

This paper includes data collected by the TESS mission. Funding for the TESS mission is provided by the NASA Explorer Program. Funding for the TESS Asteroseismic Science Operations Centre is provided by the Danish National Research Foundation (Grant agreement no.: DNRF106), ESA PRODEX (PEA 4000119301) and Stellar Astrophysics Centre (SAC) at Aarhus University. We acknowledge the use of public TESS data from pipelines a the TESS Science Office and at the TESS Science Processing Operations Center. Resources supporting this work were provided by the NASA High-End Computing (HEC) Program through the NASA Advanced Supercomputing (NAS) Division at Ames Research Center for the production of the SPOC data products.

REFERENCES

Aerts, C., Christensen-Dalsgaard, J., & Kurtz, D. W. 2010, Asteroseismology, Astronomy and Astrophysics Library (Dordrecht: Springer Netherlands), doi: 10.1007/978-1-4020-5803-5

Aerts, C., Mathis, S., & Rogers, T. M. 2019, Annual Review of Astronomy and Astrophysics, 57, 35, doi: 10.1146/annurev-astro-091918-104359

Anderson, E. R., Duvall, Thomas L., J., & Jefferies, S. M. 1990, ApJ, 364, 699, doi: 10.1086/169452

Auvergne, M., Bodin, P., Boisnard, L., et al. 2009, Astronomy & Astrophysics, 506, 411, doi: 10.1051/0004-6361/200810860

Baglin, A., Auvergne, M., Boisnard, L., et al. 2006, in 36th COSPAR Scientific assembly, Vol. 36, 3749

Bedding, T. R., Huber, D., Stello, D., et al. 2010, ApJL, 713, L176, doi: 10.1088/2041-8205/713/2/L176

Bedding, T. R., Mosser, B., Huber, D., et al. 2011, Nature, 471, 608, doi: 10.1038/nature09935

Bétrisey, J., & Buldgen, G. 2022, Astronomy and Astrophysics, 663, A92, doi: 10.1051/0004-6361/202243640

Borucki, W. J., Koch, D., Basri, G., et al. 2010, Science, 327, 977, doi: 10.1126/science.1185402

Chaplin, W. J., Kjeldsen, H., Bedding, T. R., et al. 2011, The Astrophysical Journal, 732, 54, doi: 10.1088/0004-637X/732/1/54

Chaplin, W. J., Basu, S., Huber, D., et al. 2014, The Astrophysical Journal Supplement Series, 210, 1, doi: 10.1088/0067-0049/210/1/1

Christensen-Dalsgaard, J. 1984, in Space Research in Stellar Activity and Variability, ed. A. Mangeney & F. Praderie, 11

Christensen-Dalsgaard, J., Silva Aguirre, V., Elsworth, Y., & Hekker, S. 2014, MNRAS, 445, 3685, doi: 10.1093/mnras/stu2007

Corsaro, E., De Ridder, J., & García, R. A. 2015, A&A, 579, A83, doi: 10.1051/0004-6361/201525895

Corsaro, E., Stello, D., Huber, D., et al. 2012, ApJ, 757, 190, doi: 10.1088/0004-637X/757/2/190

Deheuvels, S., Ballot, J., Eggenberger, P., et al. 2020, Astronomy and Astrophysics, 641, A117, doi: 10.1051/0004-6361/202038578

Deheuvels, S., Ballot, J., Gehan, C., & Mosser, B. 2022, A&A, 659, A106, doi: 10.1051/0004-6361/202142094

Deheuvels, S., Doğan, G., Goupil, M. J., et al. 2014, Astronomy and Astrophysics, 564, A27, doi: 10.1051/0004-6361/201322779

Foreman-Mackey, D., Hogg, D. W., Lang, D., & Goodman, J. 2013, PASP, 125, 306, doi: 10.1086/670067

Fuller, J., Cantiello, M., Stello, D., Garcia, R. A., & Bildsten, L. 2015, Science, 350, 423, doi: 10.1126/science.aac6933

Gehan, C., Mosser, B., Michel, E., Samadi, R., & Kallinger, T. 2018, A&A, 616, A24, doi: 10.1051/0004-6361/201832822

Gough, D. O. 1986, in Hydrodynamic and Magnetodynamic Problems in the Sun and Stars, ed. Y. Osaki, 117

Goupil, M. J., Mosser, B., Marques, J. P., et al. 2013, A&A, 549, A75, doi: 10.1051/0004-6361/201220266

Handberg, R., & Campante, T. L. 2011, Astronomy & Astrophysics, 527, A56, doi: 10.1051/0004-6361/201015451

Hatt, E., Nielsen, M. B., Chaplin, W. J., et al. 2023, Astronomy & Astrophysics, 669, A67, doi: 10.1051/0004-6361/202244579

Hekker, S., Gilliland, R. L., Elsworth, Y., et al. 2011, Monthly Notices of the Royal Astronomical Society, 414, 2594, doi: 10.1111/j.1365-2966.2011.18574.x

Hon, M., Huber, D., Kuszlewicz, J. S., et al. 2021, The Astrophysical Journal, 919, 131, doi: 10.3847/1538-4357/ac14b1

Howell, S. B., Sobeck, C., Haas, M., et al. 2014, Publications of the Astronomical Society of the Pacific, 126, 398, doi: 10.1086/676406

Huber, D., Bedding, T. R., Stello, D., et al. 2010, The Astrophysical Journal, 723, 1607, doi: 10.1088/0004-637X/723/2/1607

Huber, D., Silva Aguirre, V., Matthews, J. M., et al. 2014, The Astrophysical Journal Supplement Series, 211, 2, doi: 10.1088/0067-0049/211/1/2

Jenkins, J. M. 2017, Kepler Data Processing Handbook: Overview of the Science Operations Center, Tech. rep.

Kallinger, T., Mosser, B., Hekker, S., et al. 2010, Asteroseismology of Red Giants from the First Four Months of Kepler Data: Fundamental Parameters, doi: 10.1051/0004-6361/201015263

Kallinger, T., Hekker, S., Mosser, B., et al. 2012, Astronomy and Astrophysics, 541, A51, doi: 10.1051/0004-6361/201218854

Kallinger, T., De Ridder, J., Hekker, S., et al. 2014, Astronomy & Astrophysics, 570, A41, doi: 10.1051/0004-6361/201424313

Kuszlewicz, J. S., Hon, M., & Huber, D. 2023, The Astrophysical Journal, 954, 152, doi: 10.3847/1538-4357/ace598

Li, G., Deheuvels, S., & Ballot, J. 2024, A&A, 688, A184, doi: 10.1051/0004-6361/202449882

Li, G., Deheuvels, S., Ballot, J., & Lignières, F. 2022, Nature, 610, 43, doi: 10.1038/s41586-022-05176-0

Li, G., Deheuvels, S., Li, T., Ballot, J., & Lignières, F. 2023a, A&A, 680, A26, doi: 10.1051/0004-6361/202347260

Li, Y., Bedding, T. R., Li, T., et al. 2020, Monthly Notices of the Royal Astronomical Society, 495, 2363, doi: 10.1093/mnras/staa1335

Li, Y., Bedding, T. R., Stello, D., et al. 2023b, MNRAS, 523, 916, doi: 10.1093/mnras/stad1445

Lund, M. N., Silva Aguirre, V., Davies, G. R., et al. 2017, ApJ, 835, 172, doi: 10.3847/1538-4357/835/2/172

Mathur, S., García, R. A., Huber, D., et al. 2016, The Astrophysical Journal, 827, 50, doi: 10.3847/0004-637X/827/1/50

Mosser, B., Pinçon, C., Belkacem, K., Takata, M., & Vrard, M. 2017, A&A, 600, A1, doi: 10.1051/0004-6361/201630053

Mosser, B., Goupil, M. J., Belkacem, K., et al. 2012a, A&A, 548, A10, doi: 10.1051/0004-6361/201220106

—. 2012b, A&A, 540, A143, doi: 10.1051/0004-6361/201118519

Ong, J. M. J., & Basu, S. 2019, The Astrophysical Journal, 885, 26, doi: 10.3847/1538-4357/ab425f

Ong, J. M. J., Lindsay, C. J., Reyes, C., Stello, D., & Roxburgh, I. W. 2025, Resolving an Asteroseismic Catastrophe: Structural Diagnostics from p-Mode Phase Functions off the Main Sequence, arXiv, doi: 10.48550/arXiv.2501.05343

Osaki, Y., & Shibahashi, H. 1990, Progress of Seismology of the Sun and Stars, Vol. 367, doi: 10.1007/3-540-53091-6

Ricker, G. R., Winn, J. N., Vanderspek, R., et al. 2015, Journal of Astronomical Telescopes, Instruments, and Systems, 1, 014003, doi: 10.1117/1.JATIS.1.1.014003

Roxburgh, I. W., & Vorontsov, S. V. 2003, Astronomy & Astrophysics, 411, 215, doi: 10.1051/0004-6361:20031318

Rui, N. Z., & Fuller, J. 2021, MNRAS, 508, 1618, doi: 10.1093/mnras/stab2528

Schofield, M., Chaplin, W. J., Huber, D., et al. 2019, ApJS, 241, 12, doi: 10.3847/1538-4365/ab04f5

Shibahashi, H. 1979, PASJ, 31, 87

Stello, D., Cantiello, M., Fuller, J., et al. 2016, Nature, 529, 364, doi: 10.1038/nature16171

Stello, D., Huber, D., Bedding, T. R., et al. 2013, The Astrophysical Journal, 765, L41, doi: 10.1088/2041-8205/765/2/L41

Stello, D., Saunders, N., Grunblatt, S., et al. 2022, Monthly Notices of the Royal Astronomical Society, 512, 1677, doi: 10.1093/mnras/stac414

Tassoul, M. 1980, ApJS, 43, 469, doi: 10.1086/190678

Twicken, J. D., Jenkins, J. M., Seader, S. E., et al. 2016, The Astronomical Journal, 152, 158, doi: 10.3847/0004-6256/152/6/158

Unno, W., Osaki, Y., Ando, H., & Shibahashi, H. 1979, Nonradial oscillations of stars

VanderPlas, J. T. 2018, The Astrophysical Journal Supplement Series, 236, 16, doi: 10.3847/1538-4365/aab766

Vrard, M., Kallinger, T., Mosser, B., et al. 2018, Astronomy & Astrophysics, 616, A94, doi: 10.1051/0004-6361/201732477

Vrard, M., Pinsonneault, M. H., Elsworth, Y., et al. 2024, arXiv e-prints, arXiv:2411.03101, doi: 10.48550/arXiv.2411.03101

Wang, Y., Li, T., Bi, S., Bedding, T. R., & Li, Y. 2023, ApJ, 953, 182, doi: 10.3847/1538-4357/ace4c9

White, T. R., Bedding, T. R., Stello, D., et al. 2011, The Astrophysical Journal, 743, 161, doi: 10.1088/0004-637X/743/2/161

White, T. R., Bedding, T. R., Stello, D., et al. 2011, ApJL, 742, L3, doi: 10.1088/2041-8205/742/1/L3

Yu, J., Huber, D., Bedding, T. R., et al. 2018, The Astrophysical Journal Supplement Series, 236, 42, doi: 10.3847/1538-4365/aaaf74

—. 2016, Monthly Notices of the Royal Astronomical Society, 463, 1297, doi: 10.1093/mnras/stw2074

Zhou, J., Bi, S., Yu, J., et al. 2024, ApJS, 271, 17, doi: 10.3847/1538-4365/ad18db